

A MULTI-PEAK SOLAR FLARE WITH A HIGH TURNOVER FREQUENCY OF THE GYROSYNCHROTRON SPECTRA FROM THE LOOP-TOP SOURCE

ZHAO WU,^{1,2} ALEXEY KUZNETSOV,³ SERGEY ANFINOGENOV,³ VICTOR MELNIKOV,⁴ ROBERT SYCH,³
BING WANG,² RUIHENG ZHENG,¹ XIANGLIANG KONG,¹ BAOLIN TAN,⁵ ZONGJUN NING,⁶ AND
YAO CHEN^{1,2,7}

¹*School of Space Science and physics, Shandong University, Weihai, Shandong 264209, China; yaochen@sdu.edu.cn*

²*Laboratory for Electromagnetic Detection, Institute of Space Sciences, Shandong University, Weihai, Shandong 264209, China*

³*Institute of Solar-Terrestrial Physics, Irkutsk 664033, Russia*

⁴*Central Astronomical Observatory at Pulkovo of the Russian Academy of Sciences, 196140 St Petersburg, Russia*

⁵*CAS Key Laboratory of Solar Activity, National Astronomical Observatories, Chinese Academy of Sciences, Beijing 100101, China*

⁶*Key Laboratory of Dark Matter and Space Science, Purple Mountain Observatory, Chinese Academy of Sciences, Nanjing 210023, China*

⁷*Institute of Frontier and Interdisciplinary Science, Shandong University, Qingdao, Shandong 266237, China*

ABSTRACT

The origin of multiple peaks in lightcurves of various wavelengths remains illusive during flares. Here we discuss the flare of SOL2023-05-09T03:54M6.5 with six flux peaks as recorded by a tandem of new microwave and Hard X-ray instruments. According to its microwave spectra, the flare represents a high-turnover frequency (>15 GHz) event. The rather-complete microwave and HXR spectral coverage provides a rare opportunity to uncover the origin of such event together with simultaneous EUV images. We concluded that (1) the microwave sources originates around the top section of the flaring loops with a trend of source spatial dispersion with frequency; (2) the visible movement of the microwave source from peak to peak originates from the process of new flaring loops appearing sequentially along the magnetic neutral line; 3) the optically-thin microwave spectra are hard with the indices (α_{tn}) varying from ~ -1.2 to -0.4 , and the turnover frequency always exceeds 15 GHz; 4) higher turnover/peak frequency corresponds to stronger peak intensity and harder optically-thin spectra. Using the Fokker-Planck and GX simulator codes we obtained a good fit to the observed

microwave spectra and spatial distribution of the sources at all peaks, if assuming the radiating energetic electrons have the same spatial distribution and single-power-law spectra but with the number density varying in a range of $\sim 30\%$. We conclude that the particle acceleration in this flare happens in a compact region nearing the looptop. These results provide new constraints on the acceleration of energetic electrons and the underlying flare intermittent reconnection process.

Keywords: Solar flares, Solar radio emission, Solar magnetic reconnection, Solar energetic particles, Solar corona

1. INTRODUCTION

Solar flares often manifest multiple peaks in their light curves of microwave and hard X-ray (HXR) emissions. The underlying physics for these peaks remains ambiguous, and may vary from event to event. Such events are often classified as quasi-periodic pulsations (QPP) events, if the peaks present obvious periodicity (e.g. [Nakariakov & Melnikov 2009](#); [Zimovets et al. 2021](#); [Li & Chen 2022](#)). Possible mechanisms include the modulation of emission and energy release by magnetohydrodynamic (MHD) waves ([Reznikova et al. 2010](#); [Mclaughlin et al. 2018](#)), the self oscillation caused by steady inflow towards the reconnection site ([Nakariakov et al. 2010](#)), and intermittent reconnection (e.g. [Li & Gan 2006](#); [Ofman et al. 2011](#); [Liu et al. 2013](#); [Kim et al. 2013](#); [Wu et al. 2016](#)). [Ning et al. \(2018\)](#) investigated the flare of SOL2016-07-24T06:20 with double HXR peaks. They concluded the peaks are due to a two-stage energy release process, with the first peak being non-thermal due to energetic electrons accelerated via the loop-loop reconnection, and the second peak being thermally-dominated due to direct heating through the loop-loop reconnection at a relatively high altitude. This means the peaks may have distinct physical origin. These studies reveal the complex physical nature underlying the radiation peaks of solar flares.

Analysis combining the microwave and HXR data is essential to probe the physics of flares (e.g. [White et al. 2011](#); [Chen et al. 2016, 2017](#); [Gary et al. 2018](#); [Nindos 2020](#); [Krucker et al. 2020](#)). A tandem of instruments have been developed to do this, including: 1) the Siberian RadioHeliograph (SRH, [Altyntsev et al. 2020](#)) with three separated sub-arrays in bands of 3-6, 6-12, and 12-24 GHz, with test observation starting since March 2021 and regular observation since December 2023; 2) the Chashan Broadband Solar millimeter spectrometer (CBS, [Shang et al. 2022, 2023](#)), recording the dynamic spectra from 35 to 40 GHz; 3) the Hard X-Ray Imager (HXI, [Su et al. 2019](#)) on board the Advanced Space-based Solar Observatory (ASO-S, [Gan et al. 2023](#)), providing the HXR data from 10 to 300 keV; 4) the Nobeyama Radiopolarimeter (NoRP, [Nakajima et al. 1985](#)), measuring the microwave flux density at 7 discrete frequencies from 1 to 80 GHz; and 5) Konus-Wind (KW, [Lysenko et al. 2022](#)), recording the HXR flux in energy range of ~ 18 keV-1.3 MeV.

With the CBS and NoRP data, [Yan et al. \(2023\)](#) reported similar spectral properties of flare peaks observed during the X2.2 flare on 2022 April 20. The event has a high turnover frequency (ν_t) of its microwave gyrosynchrotron spectrum that extends from 20 GHz to >40 GHz during the impulsive stage. They reported a power-law dependence of the turnover flux I_t on the turnover or peak frequency ν_t , and identified the rapid-hardening-then-softening trend within the optically-thin regime of the gyrosynchrotron (GS) radiation. Usual GS spectra of flares present a reversed-V shape, with flux density peaking at ν_t that is ~ 5 -10 GHz for average events. Flares with a high turnover frequency (>15-20 GHz) are of particular interest since this indicates the abundance of mildly-relativistic electrons spiraling within a relatively strong magnetic field (e.g. [White et al. 1992](#); [Nagnibeda et al. 2013](#); [Song et al. 2016](#); [Wu et al. 2019](#)). No microwave imaging data are available for the event. This limits further analysis of the radiation sources.

Here we focus on the M6.5 class flare on 2023 May 9 that has been well observed by the instruments mentioned above, with imaging data being available. During its impulsive stage the flare manifests 6 peaks in its microwave and HXR flux curves, all these peaks are characterized by high-turnover frequency. This provides a rare opportunity of further investigation of such event.

2. DATA AND EVENT OVERVIEW

2.1. *Instruments and Data*

The microwave images were observed by the low- (3 – 6 GHz) and middle-frequency (6 – 12 GHz) SRH arrays, with the time resolution of ~ 3.5 seconds, spatial resolution of 15 – 30'' and 12 – 24'', and spectral resolution of 0.2 and 0.4 GHz. Note that the spatial resolution only means the smallest details that can be resolved, and the centroid position can be estimated with an error (σ) within a fraction of a beam width (e.g. [Condon 1997](#); [Yu et al. 2024](#))

$$\sigma \approx \frac{\theta}{2\text{SNR}\sqrt{\ln 2}}, \quad (1)$$

where θ is the half-power beamwidth of the beam size, and SNR is the signal to noise ratio of the synthesized images (typically ~ 1000 for SRH).

To minimize the instrumental shifts that may arise in the interferometric images, we further aligned the SRH microwave sources with the features visible in other spectral ranges (in particular, in magnetograms). We created a model with the magnetogram (at 03:48 UT) of the nearby non-flaring active region AR 13297, using the GX Simulator code (Nita et al. 2023) and the technique described by Fleishman et al. (2021). We derived position deviations (i.e., effectively, the differences between the observed and model source centroid positions, because the considered active region was only partially resolved with the SRH) for each frequency with cross-correlation of SRH observations and synthetic images of gyroresonance emission. We then applied the shifts required to remove these deviations (assuming them being constant with time) to all SRH images throughout the flare. The described procedure also allowed us to obtain a more accurate mutual alignment of the SRH images at different frequencies.

The following spectral data were used: 1) the NoRP radio flux densities at 1, 2, 3.75, 9.4, 17, and 35 GHz; 2) the integrated radio flux densities from the flaring region of the above SRH images; 3) the CBS radio flux densities from 35.25 to 39.75 GHz with steps of 500 MHz.

We analyzed HXR light curves recorded by HXI at discrete bands (10 – 20, 20 – 50, 50 – 100, and 100 – 300 keV), and by the KW at 18 – 80 and 80 – 328 keV. We also used the Soft X-Ray (SXR) data recorded by the GOES satellites at 0.5 – 4.0 and 1 – 8 Å.

2.2. Event Overview

The M6.5 flare on 2023 May 9 originated from the NOAA Active Region (AR) 13296 on the solar disk. According to the GOES SXR fluxes (solid lines in Figure 1(a)), the eruption started at \sim 03:36 UT, and peaked at \sim 03:54 UT. The temporal profiles of both SXR fluxes and their corresponding time derivatives (dashed lines in Figure 1(a)) manifest slight bumps around 03:40 UT, and significant enhancements around 03:54 UT. We can split the event into the pre-impulsive stage (\sim 03:36-03:46 UT), the impulsive stage (\sim 03:46-03:55 UT), and the gradual stage (after 03:55 UT).

Figure 2 shows the dynamic evolution with AIA images at 94 Å. During the pre-impulsive stage (Figure 2(a)), two sets of loops (pointed by arrows) meet and reconnect after \sim 03:36 UT, generating a large-scale coronal loop system (red arrows in Figure 2(b)). These new loops rise and approach

the southwestern loops (orange arrows), leading to sequential reconnection around the “ X ” point (Figure 2(c)) during the impulsive stage. Then the loops (blue arrow in Figure 2(d)) erupt, and sequential brightening appears along the neutral line between reconnecting loops (NL in Figure 2(d)). According to the magnetogram data (Figure 2(e)), the footpoints of the flare loops have opposite magnetic polarities, being associated with a pair of Ultraviolet (UV 1600 Å) ribbons (R_1 & R_2 , Figure 2(f)).

Figure 1 presents the microwave and HXR data. According to the microwave temporal profiles, the flux densities above ~ 9.4 GHz exceed 1000 SFU, and those above 35 GHz reach up to ~ 3000 SFU (see Figure 1(b) and (c)). Six distinct local peaks (black arrows in Figure 1(c), marked as $P_1 - P_6$) can be identified from 03:51 to 03:53 UT and appear in all microwave flux curves. The intervals between these peaks are 22s, 17s, 9s, 16s, and 9s, without significant periodicity. This is why we do not classify this flare as a QPP event. The peaks are more prominent at frequencies higher than 10 GHz. The HXR fluxes above ~ 100 keV are 1-2 orders of magnitude above the corresponding background values, with similar peaks (Figure 1(d)).

From Figure 1(c) the flux densities at 17 GHz (orange dashed) are close to those at 35 GHz (green dashed) at all local peaks. This indicates that the microwave spectral peak/turnover frequency should lie around or exceed 17 GHz. In other words, the current event belongs to flares with a high turnover frequency (c.f., Yan et al. 2023).

3. ANALYSIS OF THE MULTI-PEAK RADIATION

3.1. *The Main Peak*

We first pay attention to the highest peak (P_2) around 03:51:53 UT. Figure 3(a) presents the 94 Å image observed at 03:51:59 UT, overlaid with microwave sources (filled contours). The microwave sources appear between the two UV ribbons (R_1 and R_2), being co-spatial with the top-cusp of top section of the flare loop. Such type of the observed microwave brightness distribution, with the maximum brightness close to the looptop can be explained by effects of localized injection and transverse pitch-angle anisotropy of accelerated high-energy electrons as well as by possible high

optical thickness of the microwave source in the looptop where magnetic field strength is minimal (e.g. Melnikov et al. 2002; Kuznetsov & Kontar 2015).

We observe some spatial separation among these microwave sources (see filled contours in Figure 3(a)). In the lower-frequency range (From ~ 2.8 to ~ 6.6 GHz), the sources manifest regular spatial dispersion with frequency, with lower-frequency sources locating to the left and higher-frequency sources locating to the right. The source spacing between 2.8 (orange) and 6.6 GHz (cyan) reaches up to $\sim 10''$. The higher-frequency sources at 6.6 (cyan), 9.0 (blue), and 10.2 GHz (black) overlap with each other, and are closer to the right ribbon R_2 . These sources together agree with the overall looptop morphology of the flare. The overlap of higher-frequency sources may stem from the projection effect near R_2 .

We further perform a spectral fitting (e.g. see function in Ning & Ding 2007; Asai et al. 2013) of the spatially-unresolved nonthermal microwave spectra observed by SRH, NoRP, and CBS. We note that significant error may arise from data discrepancies among instruments due to their different calibration methods. To constrain systematic errors, we cross-calibrate the SRH and CBS data with the NoRP ones measured at the same frequency: we multiply the SRH fluxes with the ratio of NoRP to SRH values at 9.4 GHz, and the CBS fluxes with the ratio of NoRP to CBS values at 35 GHz. The fitted results (see Figure 3(b)) are representative of typical gyrosynchrotron spectra (solid lines) with large turnover frequencies (ν_t) of > 15 GHz (filled circle). At 03:51:34, 03:51:53, and 03:52:01 UT, ν_t is ~ 15.1 , 20.3, and 16.0 GHz, and the turnover (peak) flux I_t is ~ 1107 , 2800, and 2035 SFU, respectively. The optically thin spectra are very hard at the three moments, with index α_{tn} being -0.77 , -0.48 , and -0.58 , respectively, presenting an overall soft-hard-soft spectral pattern.

3.2. Other Peaks

In Figure 4(a)-(e), we overplot the microwave contours on EUV images observed around other peaks. Their characteristics are similar to those of the major peak: 1) the microwave sources are between the corresponding flare loop footpoints; 2) sources at lower frequency present spatial dispersion, while sources at frequency above ~ 6.6 GHz overlap and are closer to R_2 .

Figure 4(f)-(h) presents the fitted gyrosynchrotron spectra for 9 selected moments (see arrows in Figure 1(c)). During the first peak, the fitted spectra reveal that ν_t increases from 12.8 GHz at V_0 to 15.4 GHz at P_1 , and α_{tn} varying from -1.12 at V_0 to -0.75 at P_1 , with increasing flux density. For other peaks, ν_t (GHz) and α_{tn} are 15.4 and -0.75 at P_1 , 17.1 and -0.54 at P_3 , 16.0 and -0.57 at P_4 , 15.0 and -0.67 at P_5 , and 14.5 and -0.71 at P_6 , respectively. We see that α_{tn} manifests a general decreasing trend from P_3 to P_6 .

We conclude that all these peaks (including the major peak (P_2)) present similar properties with high turnover frequency ($\nu_t > 15$ GHz) and hard optically-thin spectra with α_{tn} being larger than -0.8 .

3.3. Source and spectral evolution

We now analyze the overall evolution of the emission sources during the impulsive stage. Figure 5 shows the microwave contours overplotted on AIA 94 Å images at 4.0 (a) and 10.2 (b) GHz, at the six local peaks. We observe systematic source movements from northwest to southeast from 03:51:31 UT to 03:52:44 UT, coinciding with the sequential EUV brightenings along photospheric magnetic field neutral line NL (see Figure 2 and the accompanying animation). The moving distance decreases with increasing frequency. For instance, the source centroid moves $\sim 15 - 20''$ at 4.0 GHz (see Figure 5(a)), and $\sim 5 - 10''$ at 10.2 GHz (Figure 5(b)). The visible movement of the microwave source from peak to peak possibly originates from the process of new flaring loops appearing sequentially along the NL . A similar process was reported for the flare 22 Aug 2005 (Reznikova et al. 2010)

In Figure 6, we show the evolution of the fitted spectral parameters (α_{tn} , ν_t , and I_t) from 03:51 to 03:53 UT. During the whole impulsive stage ν_t is close to or above ~ 15 GHz, and I_t exceeds ~ 2000 SFU. Both parameters correlate well with the total microwave flux densities. According to Figures 6(b) and (c), both the stronger turnover flux density (I_t) and harder optically-thin spectral slope (α_{tn}) correlate well with the higher corresponding turnover frequency (ν_t). Relation between I_t and ν_t can be fitted with a power-law dependence of $I_t \propto \nu_t^{2.05}$, with a correlation coefficient being ~ 0.72 , and that between α_{tn} and ν_t can be fitted with $\alpha_{tn} \propto -\nu_t^{-1.48}$, with a correlation coefficient being ~ 0.75 .

Around P_1 , the spectral power-law index α_{tn} increases sharply from ~ -1.1 to ~ -0.4 in about 20 s, reaching maximum around P_2 ($\sim 03:51:53$ UT). After that, α_{tn} decreases to ~ -0.7 . The overall evolution of α_{tn} manifests a weak “soft-hard-soft” (SHS) trend, with α_{tn} varying from ~ -1.12 to -0.42 . Note that the optically-thin spectra during this peak are very hard, indicating that the energetic electrons have hard energy spectra ($\sim -1.8 < \delta < \sim -2.6$), according to the empirical relation of $\delta = (\alpha_{tn} - 1.22)/0.9$ given by [Dulk \(1985\)](#). This means very efficient acceleration of high energy electrons in the flare.

We also performed the spectral fitting of the KW data (see [Figure 7](#)). This is done with a thick-target model. During the impulsive phase, the electron energy spectral index (δ_x) varies from -3.97 to -3.82 , with the maximum being at the peak P_2 and the minimum being at the peak P_1 . The δ_x undergoes a trend similar to its microwave counterpart (δ). Both the HXR and microwave spectra get hardened from P_1 to P_2 , and then get softened from P_2 to P_6 . Note that the difference between δ_x and δ is ~ 2 , agreeing with previous studies (reviewed by [White et al. 2011](#)).

4. MODELING MICROWAVE EMISSION DISTRIBUTION

We further modeled the event with the GX simulator ([Nita et al. 2023](#)), which is based on the fast gyrosynchrotron code to calculate the microwave emission ([Kuznetsov & Fleishman 2021](#)).

4.1. *Basic setting of the flux tube*

The magnetic configuration of the flare loop (see upper panel of [Figure 8\(a\)](#)) was deduced via the nonlinear force-free field (NLFFF, [Wiegmann 2007](#)) extrapolation of vector magnetogram obtained by the Helioseismic and Magnetic Imager (HMI, [Schou et al. 2012](#)) at 03:48:00 UT. We selected the central flux tube with the loop length $L \approx 2.48 \times 10^9$ cm, the looptop field strength $B_0 = 190$ G, and the left and right footpoints field strength $B_{LF} \approx 1214$ G and $B_{RF} \approx 600$ G. The loop top is $0.733L$ from the left footpoint. [Figure 8\(b\)](#) presents the values of B/B_0 along the loop. We assumed the thermal electron plasma has a temperature $T = 2 \times 10^7$ K and number density $N = 5 \times 10^9$ cm $^{-3}$, distributed along the loop according to the function prescribed by [Gary et al. \(2013\)](#).

4.2. *Modeling electron distributions along the flux tube*

To understand the origin of the observed microwave brightness distribution with the peak closer to the right footpoint, we do modeling of the spatial distribution of nonthermal electrons along a magnetic loop by solving the kinetic Fokker-Planck equation. Here we consider Fokker-Planck equation, which includes nonstationary continuous injection of particles and take into account Coulomb collisions and magnetic mirroring (Hamilton et al. 1990; Reznikova et al. 2009):

$$\begin{aligned} \frac{\partial f}{\partial t} = & -c\beta\mu \frac{\partial f}{\partial s} + c\beta \frac{d \ln B}{ds} \frac{\partial}{\partial \mu} \left[\frac{1 - \mu^2}{2} f \right] \\ & + \frac{c}{\lambda_0} \frac{\partial}{\partial E} \left(\frac{f}{\beta} \right) + \frac{c}{\lambda_0 \beta^3 \gamma^2} \frac{\partial}{\partial \mu} \left[(1 - \mu^2) \frac{\partial f}{\partial \mu} \right] + S, \end{aligned} \quad (2)$$

where $f = f(E, \mu, s, t)$ is electron distribution function of kinetic energy $E = \gamma - 1$ (in units of mc^2), pitch-angle cosine $\mu = \cos \alpha$, distance from the flaring loop center s , and time t , $S = S(E, \mu, s, t)$ is injection rate, $\beta = v/c$, v and c are electron velocity and speed of light, $\gamma = 1/\sqrt{1 - \beta^2}$ is Lorentz factor, $B = B(s)$ is magnetic field distribution along the loop, $\lambda_0 = 10^{24}/n(s) \ln \Lambda$, $n(s)$ is plasma density distribution, $\ln \Lambda$ is Coulomb logarithm.

For solving the equation, we follow the initial and boundary conditions suggested in Reznikova et al. (2009). Most of the model parameters are taken to be close to those obtained in Sections 2 and 4.1. The left part of the model loop with the negative values of s has a stronger magnetic field than the right one, and corresponds to the eastern foot of the observed loop. The injection function $S(E, \mu, s, t)$ is supposed to be a product of functions dependent only on one variable (energy E , cosine of pitch angle μ , position s , and time t): $S(E, \mu, s, t) = S_1(E) \times S_2(\mu) \times S_3(s) \times S_4(t)$, where the energy dependence is a power law: $S_1(E) = (E/E_{min})^{-\delta}$, $E_{min} = 30$ keV, with spectral index $\delta = 2.6$ that is equal to one derived from microwave spectrum; $S_2(\mu)$ is a pitch-angle distribution; $S_3(s)$ is an injection source spatial distribution: $S_3(s) = \exp(-(s - s_0)^2/s_1^2)$; $S_4(t)$ is a time dependence: $S_4(t) = \exp(-(t - t_m)^2/t_0^2)$, $t_m = 15$ s, $t_0 = 12$ s, the half-width of injection duration is 30s, similar to a single peak duration of the flare under study.

We have considered three models with the isotropic injection ($S_2(\mu) = 1$): the first one with the injection location at the looptop ($s = 0$), the second one with the injection location close to the right footpoint ($s = 0.20L$), and the third one with the injection close to the left footpoint

($s = -0.40L$). The obtained electron number density distributions along the loop for energies of electrons $E = 405$ keV at different moments of time are shown in Figure 9(a), (b), and (c), respectively.

The first model (Figure 9(a)) presents a single peak of the electron distribution at the location with minimum magnetic field strength ($s = 0$) in the rising, peak, and decay phases of the flare. This happens because electrons with large pitch-angles are accumulated in the local magnetic trap mostly around $B(s) = B_{min}$, while electrons with small pitch-angles precipitate into the dense chromosphere. Two spatially separated peaks appear for the 2nd and 3rd models (Figure 9(b) and (c)), with the minimum at the looptop. The reason for this is that energetic electrons with large pitch-angles which originally isotropically injected at the positions in one loop leg have their reflection in the opposite leg where the magnetic field strength is the same (e.g. Kuznetsov et al. 2011; Kuznetsov & Kontar 2015). The shape of the distributions remains more or less similar in case we increase Coulomb scattering by 10 times, increasing the number density of thermal plasma in the looptop up to $N = 5 \times 10^{10}$ cm⁻³.

4.3. Modeling gyrosynchrotron emission distributions

We simulate microwave emission with GX_Simulator for the three models with analytical distributions with the shapes similar to the ones obtained from Fokker-Planck simulations:

$$\begin{aligned}
 f_1(s) &= \exp(-(5s/L)^2), \\
 f_2(s) &= \exp(-(8(s/L - 0.1))^2) + \exp(-(8(s/L + 0.1))^2), \\
 f_3(s) &= \exp(-(5(s/L - 0.2))^2) + \exp(-(5(s/L + 0.25))^2),
 \end{aligned} \tag{3}$$

where f_1 , f_2 , and f_3 are the normalized spatial distributions of nonthermal electrons along the flare loop for the 1st, 2nd, and 3rd models (Figure 8(c)).

We show the simulated microwave source distributions in Figure 10. Its comparison with Figure 3(a) shows that the observed source shift to the right footpoint with frequency agrees with the first two models better than the third one. So, we conclude that the electrons are accelerated and injected

close to the top of the observed flaring loop, possibly nearing the cusp of reconnecting field lines, in the flare under study.

We further fix the prescribed electron spatial and energy distributions as those used in the 1st model, but varied the number density n_0 from 2.1×10^8 , 1.9×10^8 , to 1.7×10^8 cm⁻³ for peaks P_2 , P_3 , and P_4 , respectively.

The modeled sources (upper panels in Figure 11) concentrate around the loop top (an arrow in Figure 11(a)), agreeing with the SRH observations in Figure 3 and 4. The source separations are evident, with low-frequency sources (2.75 (black), 5.01 (blue), and 6.91 (cyan) GHz) nearing the loop top, and high-frequency sources (9.54 (green) and 12.0 (orange) GHz) being closer to the footpoint. The spacing reaches up to $\sim 5''$ between 2.75 and 12.0 GHz.

The modeled spectra also agree with the observations (lower panels in Figure 11). They present typical gyrosynchrotron patterns with large ν_t that is ~ 19 , 18, and 17 GHz for P_2 , P_3 , and P_4 , respectively, being close to those obtained above (see Figures 3 and 4).

5. SUMMARY

We reported an M6.5 solar flare occurring on 2023 May 9. The flare presents intriguing multi-peak profiles in almost all available flux densities of microwave and HXR. Six local peaks are observed during the impulsive stage, with quite similar characteristics in terms of the microwave spectra and source patterns.

In terms of the microwave images, the SRH sources lie between the two UV footpoint ribbons, corresponding to the looptop/cusp section. For most peaks, the SRH sources at lower frequencies ($< \sim 6.6$ GHz) present clear spatial dispersion, while those at higher frequencies overlap with each other. From peak to peak, these sources move from northwest to southeast on the disk over time.

In terms of the microwave spectra, the optically-thin spectral indices (α_{tn}) vary from ~ -1.2 to -0.4 , and the spectra are very hard in general with a gentle first-hardening-then-softening trend similar to the hard X-ray spectral evolution. Note, however, that there is a difference between δ_x and δ of ~ 2 , agreeing with previous studies (reviewed by White et al. 2011). The spectral turnover frequencies (ν_t) of all the temporal peaks remain in the range of $\sim 15 - 22$ GHz. The higher turnover

frequency correlates with a larger turnover flux density and a harder optically-thin spectrum, with power-law dependence of $I_t \propto \nu_t^{2.05}$, and $\alpha_{tn} \propto -\nu_t^{-1.48}$, respectively. These spectral features indicate strong acceleration of high energetic non-thermal electrons around these peaks.

According to our microwave data and GX simulations, the energy spectral index of the nonthermal electrons lies in a range of -1.8 to -2.6. Regarding the spectral turnover frequency, both the Razin effect and the self-absorption effect can affect its value (Razin 1960; Ramaty 1969). In our event, the high turnover frequency ν_t and the very-hard optically-thin spectra favours the latter effect since the larger number density of high energy electrons can shift the spectral maximum toward higher frequency, without significantly enhancing their flux density at lower frequencies (see Melnikov et al. 2008; Wu et al. 2019). This is also supported by the found positive correlation between I_t and ν_t for this event.

The observed microwave features, including spectra, source position and spatial dispersion at different frequencies have been explained using NLFFF extrapolated magnetic flux tube, Fokker-Plank equation solution for electron distribution along the magnetic tube, and GX_Simulator simulation for gyrosynchrotron emission. We conclude that the particle acceleration in this flare happens in a compact region in the right portion close to the looptop, possibly in the cusp of reconnecting magnetic field lines.

The features of all observed peaks of emission are similar and differ only in the magnitude of the flux density. It seems that all of them originate from similar flare loops with the same spatial and energy distributions of the nonthermal electrons, but with different electron number density varying in a range of $\sim 30\%$. The GS simulations suggest the peaks are generated by nonthermal electrons that concentrate around the right side of the loop-top region. The source separation for each peak at different frequencies is consistent with our GS spatial distribution modeling, according to which stronger magnetic field (being at lower altitude) favours generation of higher-frequency emission (Nindos 2020).

With observations and the simulations, we suggest that the observed multiple peaks during the impulsive stage of this flare stem from intermittent energy release and electron acceleration. The

visible movement of the microwave source from peak to peak originates from the process of new flaring loops appearance sequentially along the NL. This is supported by the observed similar movement of EUV brightenings.

This work is supported by grants of National Natural Science Foundation of China 42127804, 42074203 and 11873036, the National Key R&D Program of China under grant 2022YFF0503002 (2022YFF0503000), and by the Russian Science Foundation under grant 22-12-00308 (V.M.). A.K., S.A. and R.S acknowledge financial support by the Ministry of Science and Higher Education of the Russian Federation. We appreciate the teams of SRH, CBS, ASO-S, KW, NoRP, SDO, and GOES for their open data use policy. ASO-S mission is supported by the Strategic Priority Research Program on Space Science, the Chinese Academy of Sciences, Grant No. XDA15320000.

REFERENCES

- Altynsev, A., Lesovoi, S., Globa, M. et al., 2020, *Solar-Terrestrial Physics.*, 6, 2, 30
- Asai, A., Kiyohara, J., Takasaki, H. et al., 2013, *ApJ*, 763, 87
- Bastian, T. S., Benz, A. O. & Gary, D. E., 1998, *ARA&A*, 36, 131
- Chen, Y., Du, G., Zhao, D. et al., 2016, *ApJL*, 820, L37
- Chen, Y., Wu, Z., Liu, W. et al., 2017, *ApJ*, 843, 8
- Condon, J, 1997, *PASP*, 109, 166
- Dulk, G. A., 1985, *ARA&A*, 23, 169-224
- Fleishman, G., Anfinogentov, S., Stupishin, A. et al., 2021, *ApJ*, 909, 89
- Gan, W., Zhu, C., Deng, Y. et al., 2023, *SoPh*, 298, 68
- Gary, D., Fleishman, G. & Nita, G., 2013, *SoPh*, 288, 549
- Gary, D., Chen, B., Dennis, B. et al., 2018, *ApJ*, 863, 89
- Hamilton, R., Lu, E., & Petrosian, V. 1990, *ApJ*, 354, 726
- Kim, S., Masuda, S., Shibasaki, K. et al., 2013, *PASJ*, 65, S2
- Krucker, S., Masuda, S. & White, S., 2020, *ApJ*, 894, 158
- Kuznetsov, A., Nita, G. & Fleishman, G., 2011, *ApJ*, 742, 87
- Kuznetsov, A. & Kontar, E., 2015, *SoPh*, 290, 79
- Kuznetsov A. & Fleishman, G., 2021, *ApJ*, 922, 103
- Lee, J., 2007, *SSRv*, 133, 72
- Li, Y. & Gan, W., 2006, *ApJ*, 644, L97
- Li, D. Chen, W., 2022, *ApJL*, 931, L28

- Liu, W., Chen, Q. & Petrosian, V., 2013, *ApJ*, 767, 168
- Lysenko, A., Ulanov, M., Kuznetsov, A. et al., 2022, *ApJS*, 262, 32
- Mclaughlin, J., Nakariakov, V., Dominique, M. et al., 2018, *SSRv*, 214, 45
- Melnikov, V., Shibasaki, K., & Reznikova, V., 2002, *ApJ*, 580, L185
- Melnikov, V. F., Gary, D. E., Nita, G. M., 2008, *SoPh*, 253, 43
- Nakajima, H., Sekiguchi, H., Sawa, M. et al., 1985, *PASJ*, 37, 163
- Nakariakov, V. & Melnikov, V., 2009, *SSRv*, 149, 119
- Nakariakov, V., Inglis, A., Zimovets, I. et al., 2010, *Plasma Phys. Control Fusion*, 52, 12
- Nagnibeda, V. G., Smirnova, V. V., Ryzhov, V. S., et al. 2013, *JPhCS*, 440, 012009
- Nindos, A., 2020, *Front. Astron. Space Sci.*, 7, 57
- Ning, Z. & Ding, M., 2007, *PASJ*, 59, 373
- Ning, H., Chen, Y., Wu, Z. et al., 2018, *ApJ*, 854, 178
- Nita, G., Fleishman, G., Kuznetsov, A. et al., 2023, *ApJS*, 267, 6
- Ofman, L., Liu, W., Title, A. et al., 2011, *ApJL*, 740, L33
- Oka, M., Birn, J., Battaglia, M. et al., 2018, *SSRv*, 214, 82
- Ramaty, R., *ApJ*, 158, 753
- Razin, V.A., 1960, *Izv.VUZov.Radiofizika*, 3, 584
- Reznikova, V., Melnikov, V., Shibasaki, K. et al., 2009, *ApJ*, 697, 735
- Reznikova, V., Melnikov, V., Ji, H. et al., 2010, *ApJ*, 724, 171
- Shang, Z., Xu, K., Liu, Y. et al., 2022, *ApJS*, 258, 25.
- Shang, Z., Wu, Z., Liu, Y. et al., 2023, *ApJS*, 268, 45
- Schou, J., Scherrer, P., Bush, R. et al., 2012, *SoPh*, 275, 229
- Song, Q. W., Nakajima, H., Huang, G. L., et al. 2016, *SoPh*, 291, 3619
- Su, Y., Liu, W., Li, Y. et al., 2019, *RAA*, 19, 163
- Tan, B., 2022, *RAA*, 22, 072001
- Tian, H., Young, P., Reeves, K. et al., 2016, *ApJL*, 823, L16
- White, S. M., Kundu, M. R., Bastian, T. S., et al. 1992, *ApJ*, 384, 656
- White, S. M., Benz, A. O., Christe, S., et al., 2011, *SSRv*, 159, 225
- Wiegelmann, T, 2007, *SoPh*, 240, 227
- Wu, Z., Chen, Y., Huang, G. et al., 2016, *ApJL*, 820, L29
- Wu, Z., Chen, Y., Ning, H., et al. 2019, *ApJ*, 871, 22
- Yan, F., Wu, Z., Shang, Z. et al., 2023, *ApJL*, 942, L11
- Yu, S., Chen, B., Sharma, R. et al., 2024, *Nat. Astron.*, 8, 50
- Zimovets, I., Sharykin, I. & Myshyakov, I., 2021, *SoPh*, 296, 188

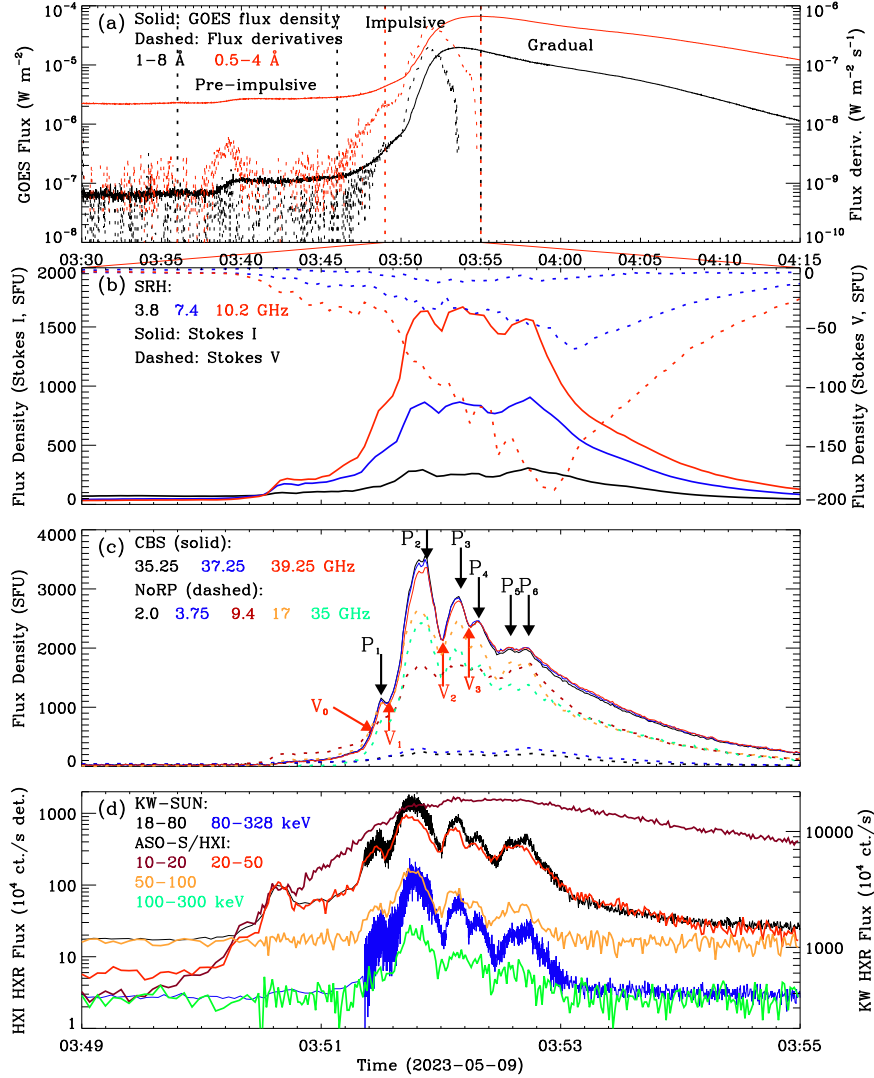


Figure 1. Flux curves of the M6.5 flare observed on May 9 2023: panel (a) the SXR fluxes (solid) and their time derivatives (dashed) observed at 1-8 Å (black) and 0.5-4 Å (red) by GOES; panel (b) the integrated total (Stokes I , solid) and polarized (Stokes V , dashed) flux density observed by SRH at 3.8 (black), 7.4 (blue) and 10.2 GHz (red); panel (c) the flux density observed by CBS (solid) at 35.25 (black), 37.25 (blue), and 39.25 (red) GHz, and by NoRP (dashed) at 2.0 (black), 3.75 (blue), 9.4 (red), 17 (orange), and 35 (green) GHz; panel (d) the HXR flux observed by HXI/ASO-S at 10-20 (brown), 20-50 (red), 50-100 (orange), and 100-300 keV (green), and by KW at 10-80 (black) and 80 - 328 keV (blue). Black arrows in panel (c) denote the local peaks of the flare, and red arrows denote the corresponding local valleys of the flux.

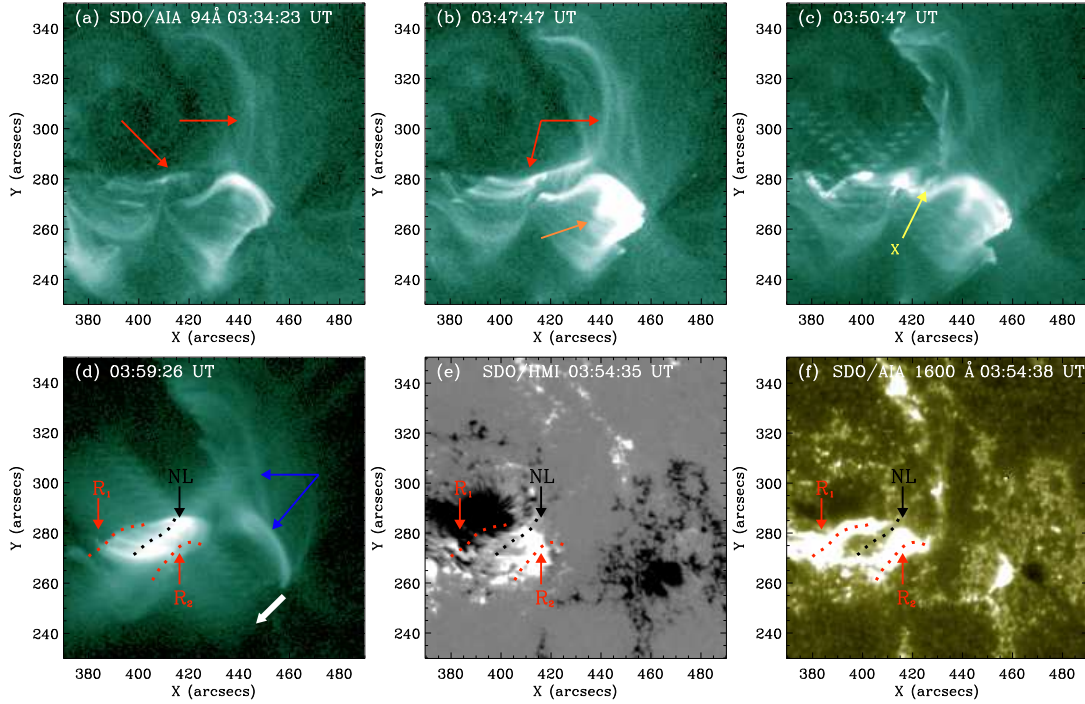


Figure 2. The AIA 94 Å images (a - d), the HMI magnetogram (e), and 1600 Å image (f). The red arrows in panel (a) point at the loops to be reconnected in the pre-impulsive stage, and the red ones in panel (b) point at the just-reconnected loop. The symbol “X” in panel (c) points at the X point of the subsequent reconnection during the impulsive stage. Panel (d) presents the erupting (blue arrows) and post-flare loops. The thick arrow (white) indicates the moving direction of the brightening loop cusps. The two red dashed line in panels (d)-(f) delineate the two UV ribbons (R_1 and R_2) and the black dashed line delineates the location of the loop cusps (NL). An animation for AIA 94 Å (for panels (a-d)) from 03:34:47 UT to 04:01:35 UT showing the dynamic evolution of the flare is available. The real-time duration of the animation is 13s.

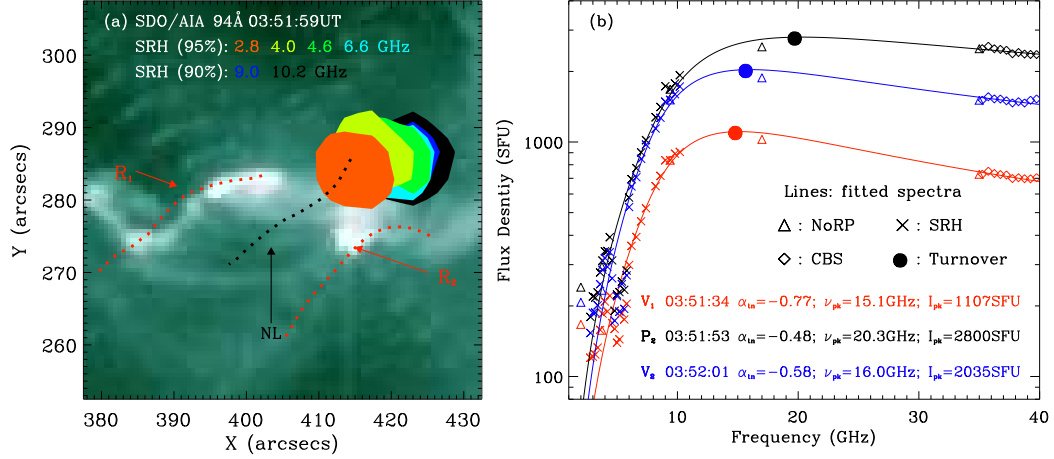


Figure 3. Imaging and spectral data around the major peak ($P_2 \sim 03:51:53$ UT) of the M6.5 flare. Panel (a) presents 94 Å image at 03:51:59 UT overlaid with the SRH microwave contours (filled) at 2.8 (orange), 4.0 (yellow), 4.6 (green), 6.6 (cyan), 9.0 (blue), and 10.2 (black) GHz. The red and black dashed lines delineate the two flare ribbons (R_1 and R_2) and magnetic field neutral line (NL) of sequential brightening, respectively. Panel (b) presents the fitted spectra of NoRP (triangle), SRH (cross), and CBS (diamond) data at three moments (corresponding to V_1 , P_1 , and V_2 in Figure 1(c)). The fitted optically-thin spectral index (α_{tn}), turnover frequency (ν_t , as filled circle), and turnover flux (I_t) are given.

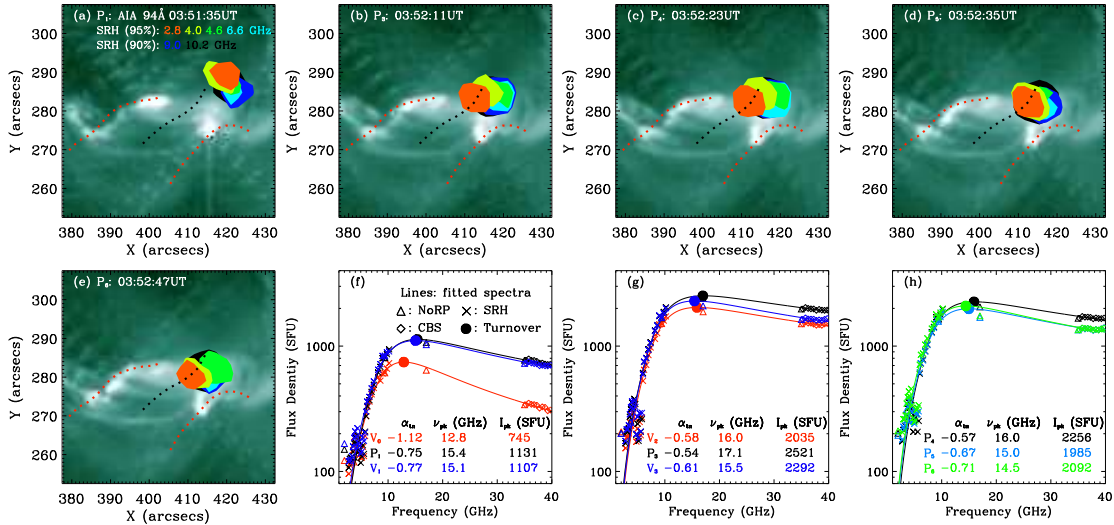


Figure 4. Same as Figure 3 but for the other five peaks (P_1 , P_3 , P_4 , P_5 , and P_6). Panels (a)-(e) show EUV images overlaid with the corresponding microwave contours. Panels (f)-(h) show the data and the fitted microwave spectra: (f) for P_1 , (g) for P_3 , and (h) for P_4 , P_5 , and P_6 .

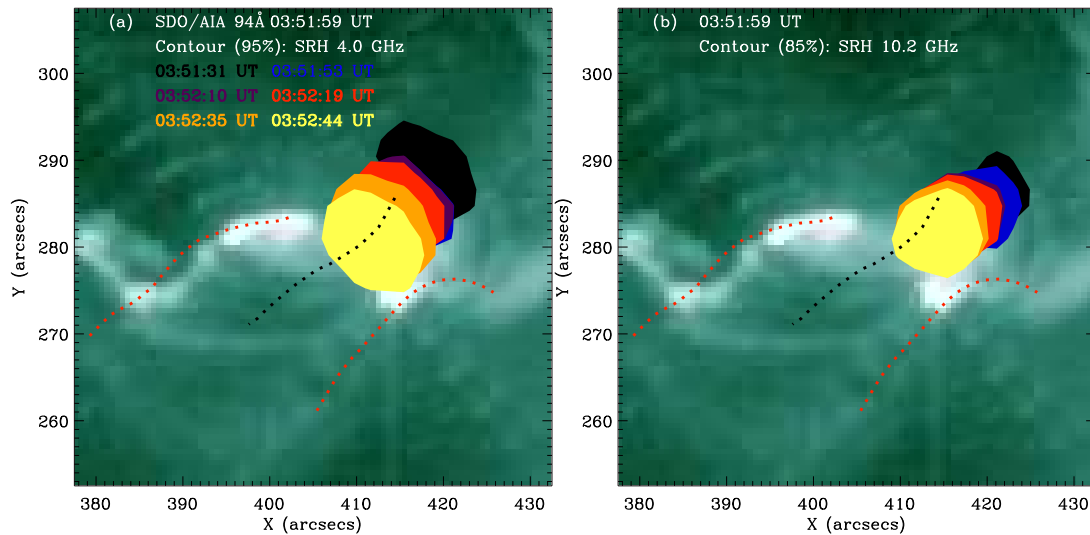


Figure 5. Motion of the microwave sources at 4.0 GHz (a) and 10.2 GHz (b) overlaid onto the SDO/AIA 94 Å image (03:51:59 UT). The SRH contours were observed at 03:51:31 (P_1 , black), 03:51:53 (P_2 , blue), 03:52:10 (P_3 , purple), 03:52:19 (P_4 , red), 03:52:35 (P_5 , orange), and 03:52:44 (P_6 , yellow) UT,.

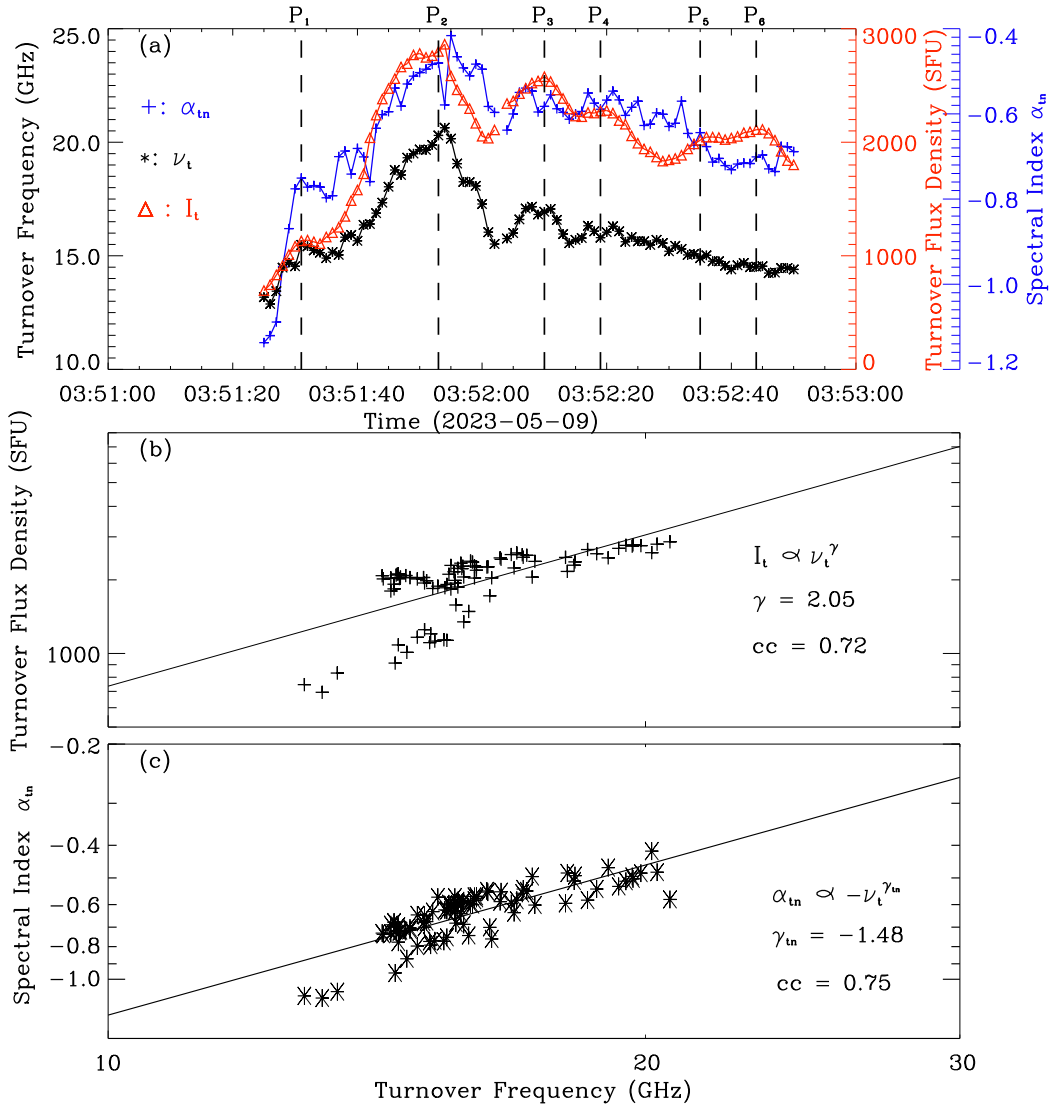


Figure 6. Evolution of the microwave spectral parameters from 03:51:00 UT to 03:53:00 UT. Panel (a) presents the fitted optically-thin spectral indices (α_{tn}), the turnover frequency and the corresponding intensity (ν_t and I_t). Panel (b) and (c) presents the fitting of I_t and α_{tn} versus ν_t , respectively. The dashed line in panels (a) denotes the local peaks.

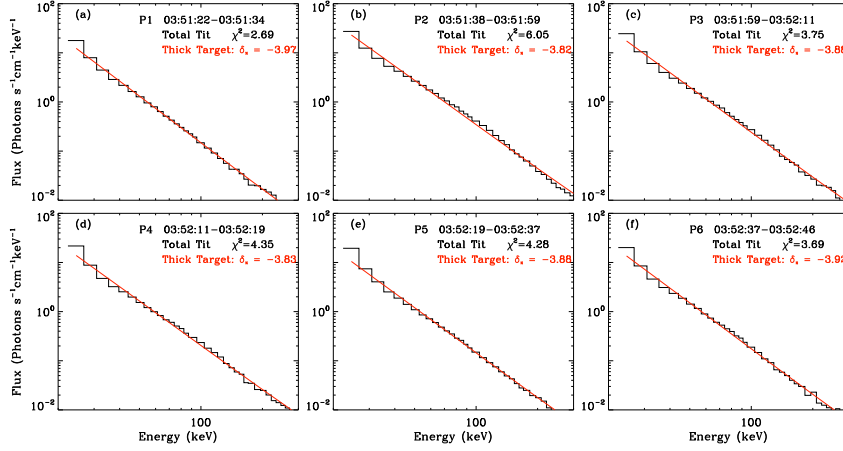


Figure 7. The HXR data of KW (black) and the thick-target spectral fitting with a single power law (red) around the flare peaks (black arrows in Figure 1(c)). The fitted parameters are written.

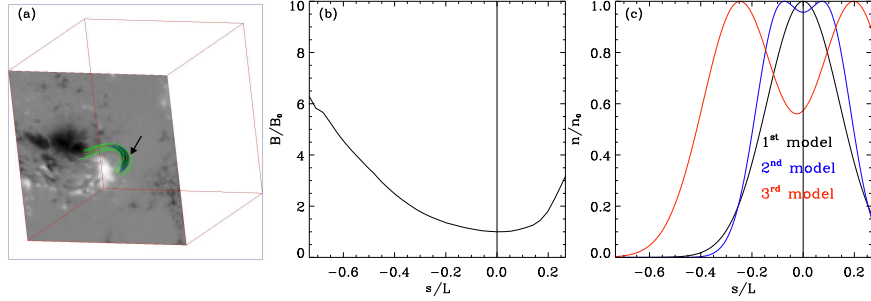


Figure 8. Parameter setup of the GX Simulator. Panel (a) presents the selected flux tube extrapolated with NLFFF extrapolation (line-of-sight view), showing the spatial distribution of nonthermal electrons as the shadowed area. Panel (b) presents the normalized magnetic field strength, and panel (c) presents the normalized density of the nonthermal electrons, along the loop. The arrow in panel (a) and vertical lines in panels (b) and (c) denote the location of the loop top.

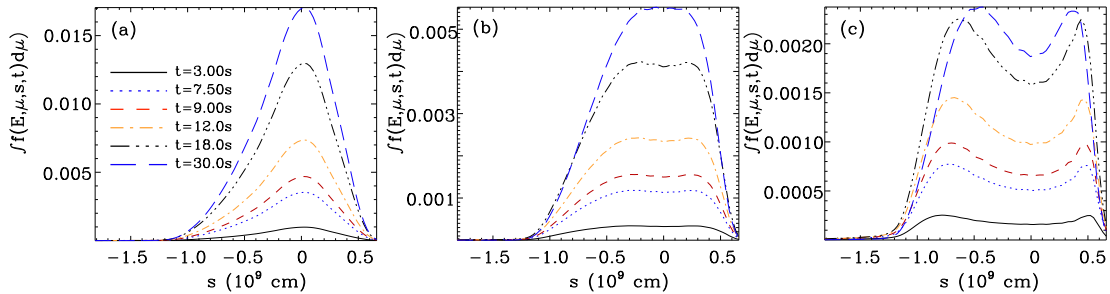


Figure 9. The simulated evolution of nonthermal electron distributions along the flux tube for the 1st (a), 2nd (b), and 3rd (c) models. The lines denote the distributions at 3.0, 7.5, 9.0, 12.0, 18.0, and 30.0s after the electron injection.

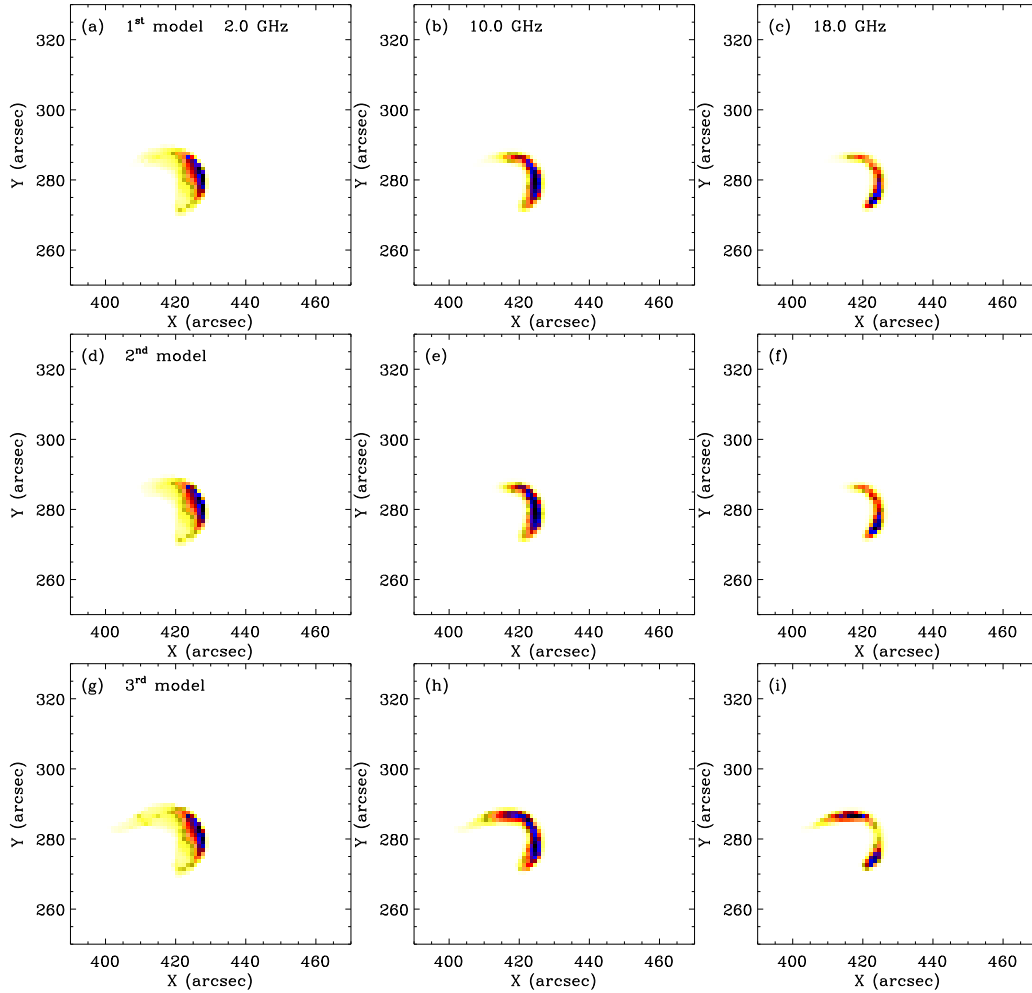


Figure 10. The simulated microwave source distributions for three models of nonthermal electrons distribution in Figure 8(c): (a)-(c) for the 1st model, (d)-(f) for the 2nd model, and (g)-(i) for the 3rd model. The left, middle and right panels present the modeled images at 2.0, 10.0, and 18.0 GHz, respectively. The maps are not convolved with the instrument beam

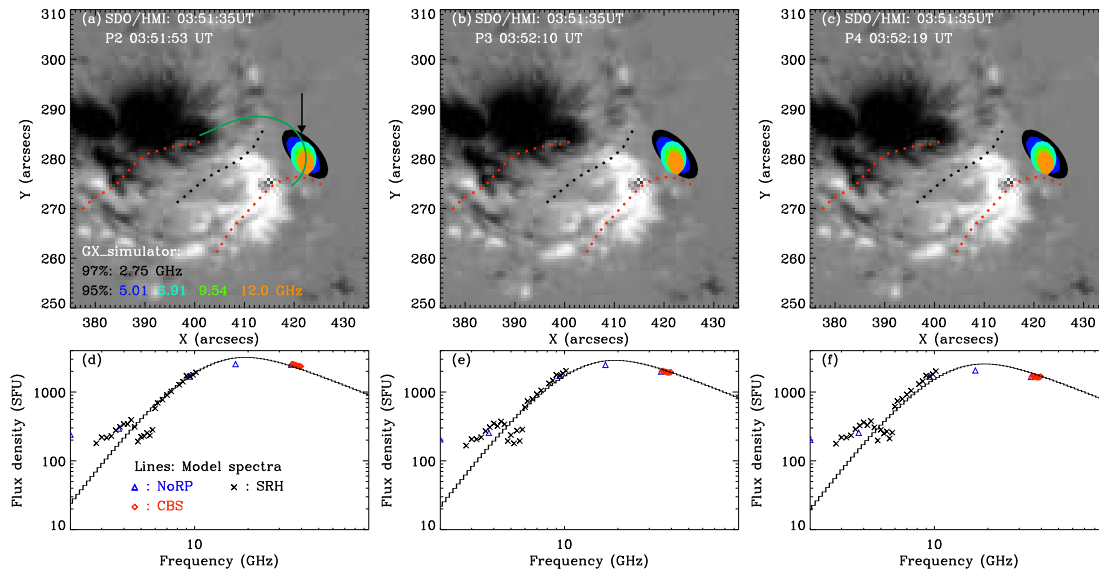


Figure 11. Upper panels (a-c): the simulated microwave sources overlaid onto the magnetogram (at 03:51:35 UT) at the 5 selected frequencies (contour level of 97% for 2.75 GHz, and 95% for 5.01, 6.91, 9.54 and 12.0 GHz). lower panels (d-f): the simulated spectra compared with the NoRP (triangles), SRH (crosses) and CBS (diamonds) data, for peaks P_2 , P_3 , and P_4 . The simulated sources have been convolved with the SRH beam at 03:52:00 UT. The green line in panel (a) depicts the central line of the modeled flux tube, and arrow points at the location of the loop top (see Figure 8).